ORIGINAL ARTICLE

# Performances of JEM-EUSO: angular reconstruction
## The JEM-EUSO Collaboration

**S. Biktemerova · A. Guzman · T. Mernik**

**Abstract** Mounted on the International Space Station(ISS), the Extreme Universe Space Observatory, on-board the Japanese Experimental Module (JEM-EUSO), relies on the well established fluorescence technique to observe Extensive Air Showers (EAS) developing in the earth's atmosphere. Focusing on the detection of Ultra High Energy Cosmic Rays (UHECR) in the decade of $10^{20}$eV, JEM-EUSO will face new challenges by applying this technique from space. The EUSO Simulation and Analysis Framework (ESAF) has been developed in this context to provide a full end-to-end simulation frame, and assess the overall performance of the detector. Within ESAF, angular reconstruction can be separated into two conceptually different steps. The first step is pattern recognition, or filtering, of the signal to separate it from the background. The second step is to perform different types of fitting in order to search for the relevant geometrical parameters that best describe the previously selected signal. In this paper, we discuss some of the techniques we have implemented in ESAF to perform the geometrical reconstruction of EAS seen by JEM-EUSO. We also conduct thorough tests to assess the performances of these techniques in conditions which are relevant to the scope of the JEM-EUSO mission. We conclude by showing the expected angular resolution in the energy range that JEM-EUSO is expected to observe.

**Keywords** JEM-EUSO · Angular reconstruction

S. Biktemerova
Joint Institute for Nuclear Research, Joliot-Curie 6, 141980 Dubna, Moscow Region, Russia
e-mail: sveta.biktemerova@gmail.com

A. Guzman (✉) · T. Mernik
Institut für Astronomie und Astrophysik Tübingen, Sand 1, 72076 Tübingen, Germany
e-mail: guzman@astro.uni-tuebingen.de

T. Mernik
e-mail: mernik@astro.uni-tuebingen.de

## 1 Introduction

### 1.1 The JEM-EUSO mission principle of operation

JEM-EUSO is a space based UV telescope devoted to the observation of ultra high energy cosmic ray (UHECR) induced air showers in the Earth's atmosphere [2]. It will be mounted on-board the Japanese Module of the International Space Station (ISS), orbiting the earth at an altitude of 400 km. Due to its instantaneous aperture of the order of $10^5 km^2 sr$, JEM-EUSO will study UHECR exceeding energies of $10^{20}$ eV with unprecedented statistics, allowing it to study the sources and their spectra with high precision [17]. The duration of the mission is scheduled to be at least 3 years. During this time, JEM-EUSO will observe several hundreds of events with energies $> 5 \times 10^{19}$ eV [11]. One of the main scientific goals of the JEM-EUSO mission is the identification of individual sources by a high-statistics arrival direction analysis. This could also allow measurements of the energy spectra of such sources, allowing production models of UHECR to be constrained. Therefore, good assessment of the incoming direction of the UHECR will be one of the key elements for the scientific success of the mission [17].

The instrument consists of the refractive optics of three Fresnel lenses focusing the UV photons onto a focal surface (FS) detector. The telescope has a cylindrical shape with a diameter of 2.65 m. The sides are cut to 1.9 m to allow the instrument to be stored inside the rocket for transfer to the ISS. The focal surface detector is made of 137 individual photo-detector modules (PDMs). Each PDM is formed by 36 multi-anode photomultiplier tubes (MAPMT). Each MAPMT has ($8 \times 8 =$) 64 pixels with an average spatial resolution of $\sim 0.5$ km projected on the earth's surface. Two levels of trigger algorithms are operated to search each PDM for stationary and transient excesses over background [1]. The telescope is equipped with an atmospheric monitoring system using LIDAR and IR-camera data to record the state of the atmosphere and infer the altitude of possible clouds inside the field of view (FOV). More details on the specifics of the detector can be found in [8, 10].

### 1.2 The EUSO Simulation and Analysis Framework (ESAF)

The EUSO Simulation & Analysis Framework (ESAF) [3] is a modular software built upon the ROOT[1] framework, designed to simulate space based UHECR detectors. The simulations account for the physical processes that take place during the development of an EAS. Each simulation covers the whole chain, the longitudinal development of the EAS itself, the fluorescence and Cerenkov light produced during the shower development, the atmospheric propagation of photons, as well as the processes within the detector, i.e. the propagation of photons through the optics, the response of the electronics, and the triggering algorithms. In a second stage, ESAF also provides the tools for reconstructing the simulated events based on the saved information from the detector's response.

---

[1] root.cern.ch/

Developed at the time of the Extreme Universe Space Observatory (EUSO) [19], ESAF is intended to simulate space based UHECR telescopes. We have reactivated the code and further enhanced it. New instrument components, such as optics and the focal surface detector have been developed and implemented in order to meet the JEM-EUSO specifications. Inter-comparison using the Offline software of the Pierre Auger Observatory have been conducted to validate the physics output for both nature and instrument [4]. We have carefully checked the inbuilt reconstruction and pattern recognition algorithms, fine tuned and partly debugged them. Additionally, alternative pattern recognition and reconstruction algorithms have been implemented.

## 1.3 UHECR event simulation with ESAF

In ESAF, there are different techniques implemented to generate or to inject EAS. In this study, we used a parametrized approach to analyze the instrument's reconstruction capability. Showers follow the Greisen Ilina Linsley (GIL) formulation, describing the distribution of charged particles along the shower axis [12]. GIL have been compared to CORSIKA/QGSJET simulations and found to be in agreement within the accuracy allowed by the Monte Carlo fluctuations [9].

Depending on the depth of the shower, Cerenkov and fluorescence photons are generated. The fluorescence photons are produced using the photon yield obtained from [18]. Even though more recent data could be used, the impact would be negligible to our experiment, since the fluctuations between the different experiments are minor [15] and out of the scope of our resolution. The atmospheric transfer of the photons is conducted via an approximation. First, the photons created at the EAS site are stored in bunches, where the number of photons per bunch depends on the altitude of the shower. Then, for each bunch absorption coefficients, as well as scattering probabilities for the Cerenkov, are assigned. These bunches are then propagated towards the detector. The validity of this method has been confirmed by [3]

At the detector level, each photon arriving at the optics is treated individually by a ray-trace through the optics. Absorption inside the optics material and scattering at the surfaces of the lenses is computed. Figure 1 shows the distribution of photons that finally reach the focal surface. Due to dead spaces between the single PDMs and the losses because of quantum efficiency, the number of photons converted to photoelectrons, and thus making signal, is further reduced by a factor of roughly 0.25. The time steps, in which this information is kept, are called gate time units (GTUs). The GTU length is fixed by JEM-EUSO's electronic response, and its nominal value is $2.5\mu$s. In our example event, the number of signal counts originated from the $10^{20}$ eV track is approx. 1000. The signal appears as a moving spot on the FS as seen in Fig. 2. It is embedded in the background of the night glow of the atmosphere. For this work, we use a value of 500 photons ns$^{-1}$m$^{-2}$sr$^{-1}$, based upon studies presented in [7].This value translates into an average of 0.44 photons per pixel per $\mu$s .The background is simulated at the electronics level, to save computing time. Otherwise, for every simulation, a huge number of background photons would have to be propagated through the optics.

Now the trigger algorithms [1] are simulated. The first trigger level works at PDM level. The *Persistent Track Trigger (PTT)* monitors groups of pixels of $3 \times 3$. The
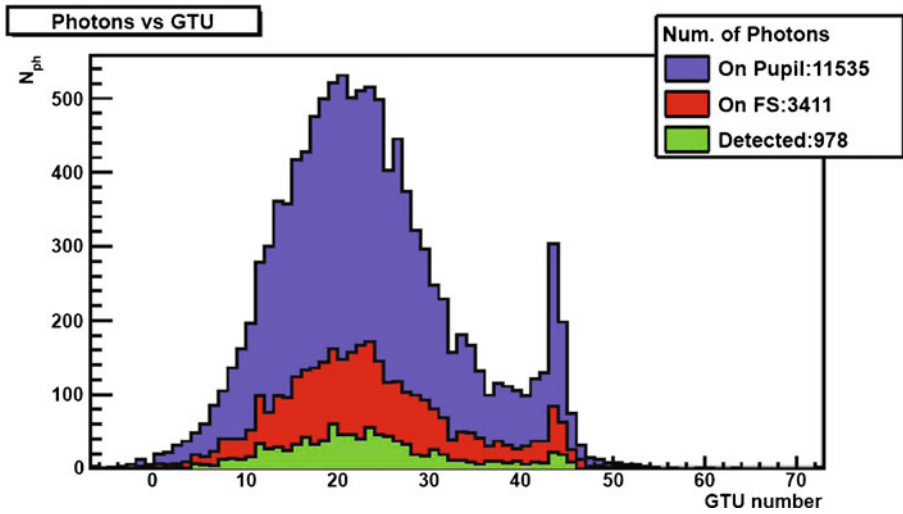
**Fig. 1** Photons coming to the detector, photons intersecting the focal surface (FS) and photons detected as function of time (in GTU). Due to the covering factor and quantum efficiency taken into account, the fraction of photons creating a signal ('Detected') is about 0.3. In this example: $10^{20}$eV proton event with 60° zenith angle
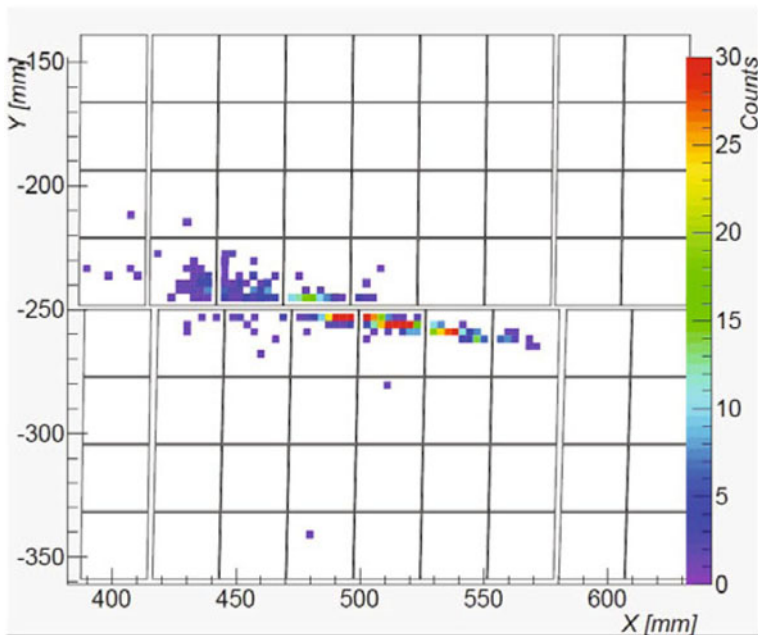


**Fig. 2** Signal track on focal surface without background displayed. Example: $10^{20}$eV proton event with 60° zenith angle

PTT is activated if for a given group of pixels, the time integrated photon count exceeds a preset threshold. The second trigger level is the *Linear Tracking Trigger* (LTT). It looks for patterns that could be signal tracks by moving an integration box along a set of predefined directions.

### 1.4 Direction reconstruction within ESAF

A precise estimation of the arrival direction of the UHECRs is among the major scientific objectives of the mission. In order to understand the accelerating mechanism and the possible sites for acceleration, one should be able to trace back the incoming primary. Nevertheless, the galactic and extragalactic magnetic fields impose a constraint on the accuracy of such a trace back. However, for the case of energies in the excess of $10^{19.7}$eV, the particle's trajectory is slightly deflected by the galactic magnetic field, assuming a proton-like composition. Thus, the EAS's track will point to the astrophysical source of the UHECR within the error induced by magnetic deflections [16]. The latter will hold even for iron-like composition at higher energies (i.e. $10^{20.4}$eV). The scientific requirement for the telescope demands an angular resolution of $< 2.5°$ for cosmic rays with energies $> 10^{20}$ eV and zenith angles $> 60°$ [21].

ESAF was developed for space borne UHECR detectors which detect and record the fluorescence and Cerenkov light produced by an EAS as it transverses the atmosphere.

This will appear as a moving signal-spot on the focal surface of such a detector.This sequence of pixels on the focal plane ordered in time and lying along some direction defines an "EAS-track". Within ESAF's modular approach, basically there are 3 reconstruction modules: the pattern recognition module, the angular reconstruction module, and the shower profile and energy reconstruction module. For the scope of this work, we shall only focus on the first two. Inside ESAF's reconstruction scheme, the information of the position on the focal surface, the timing, and intensity of the signal are used to approximate the geometrical characteristics of the EAS-track, namely the impact point at the earth's surface (if any), the azimuthal angle $\Phi$, and zenith angle $\Theta$ (see Fig. 7). Once the geometrical characteristics of the EAS have been computed, other reconstruction modules can use them to calculate the energy of the primary, the slant depth at EAS's maximum($X_{max}$), the height of the first interaction, etc.

Of particular importance, is to disentangle the background from the signal coming from the EAS. To address this issue, the JEM-EUSO instrument has a dedicated trigger technology [5] that filters the relevant information from the whole of the focal surface. Thus, the instrument keeps only information from pixels that are most likely to contain an EAS signal (Fig. 3).
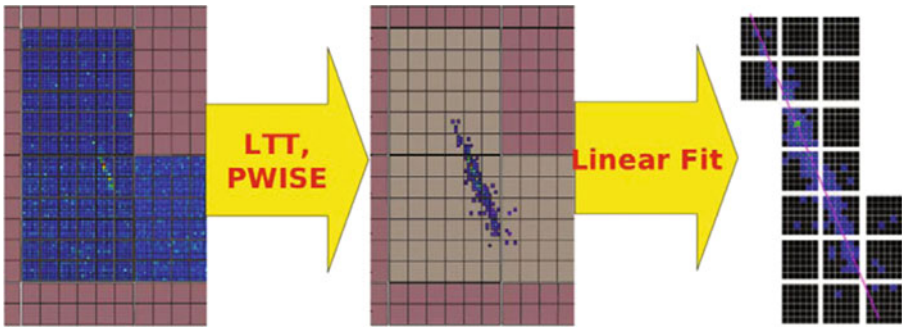
**Fig. 3** Image on the focal surface of the selected pixels (see text) and the consecutive cleansing of the signal

## 2 Pattern recognition

This module is in charge of tagging the signal counts generated by the EAS track, disentangling them from the background. Within ESAF's work-flow, pattern recognition works at a stage after the incoming photons from the telescope have already been detected and, hence, interpreted as photon-counts at the focal surface. Our basic information is the amount of detected photon-counts as a function of time for each pixel or counts per GTU. It is the job of the pattern recognition to select which of these photon-counts are to be used by the subsequent reconstruction modules.

### 2.1 The peak and window searching technique (PWISE)

This module looks at each activated pixel's photon-counts as a function of time. Using this information, it searches for photon-counts that resemble the expected behavior as the moving spot of the EAS shines upon the given pixel. It repeats this process for all activated pixels. The output of this module is a list of selected pixels, where each pixel has an associated time window(in GTUs). This time window corresponds to the expected time the shower front shone upon the selected pixel.

Besides selecting photon-counts coming from the EAS, this technique also filters out multiple-scattered photons which result in a "fuzzy" image of the track. This effect appears as a consequence of their shifted time of arrival due to the multiple scattering. The main goal driving the design of this module was to provide sufficient enough signal counts for the angular reconstruction algorithm. The idea is to optimize the performance of the angular reconstruction modules, even at the expense of losing EAS's light in the filtering process.

The key steps of the PWISE technique can be summarized as follows. At this stage, it is assumed that the information of the triggered PDMs is available:

**Step 1** For each pixel, PWISE only considers pixels whose highest photon-count (peak) is above a certain threshold (*peak-threshold*).

**Step 2**    PWISE searches for the time window with the highest signal-to-noise ratio
  SNR defined as:

$$SNR = \left( \frac{1}{\Delta\tau \cdot RMS} \right) \sum_{\Delta\tau} pc(t) \tag{1}$$

In this last expression, $pc(t)$ stands for the number of photon-counts as a function
of time, $\Delta\tau$ is the time window's width centered on this pixel's maximum peak,
and RMS is the root-mean square of the pixel's photon-counts.

**Step 3**    We check if the maximum SNR is above a given *SNR-threshold*. Only if
  the SNR is above this threshold, will we select the photon-counts within the time
  window that maximizes SNR. The selected photon-counts are then passed on to
  the next reconstruction module.

In order to estimate the ranges of the *SNR-threshold* and *peak-threshold*, we sim-
ulated events without background. This allowed us to study the SNR and peak of the
photon-counts coming from the fluorescence light produced by the EAS. As men-
tioned before, by selecting the appropriate thresholds, we select photon-counts that
most likely were produced by the EAS. Note that only a small fraction of $\Delta\tau$ can be
selected from a fixed set. This set of time windows was selected beforehand by care-
fully looking at the signal characteristics without background. As an extra feature,
we also included the possibility to select a pixel-peak, even if its SNR was not above
the *SNR-threshold*. This was done by introducing an extra *absolute-threshold*. If the
pixel-peak's counts surpass this threshold, then this pixel will be selected with a time
window of one GTU.

## 2.2 Track finding method

The track finding method is an additional algorithm in ESAF that makes it possible
to find a shower track on the focal plane.

Unlike the PWISE algorithm, in which the photon-count as a function of time for
each pixel is used, this method uses the photon-count distribution on the focal plane
at each GTU. Thus we have a "snapshot" of the focal plane with a photon-count
distribution for each GTU. The task of the algorithm is to find a point that moves
uniformly along a straight line on the focal plane using a sequence of snapshots.
The algorithm creates a set of all possible track candidates, of which the best one
is chosen. To build a track, the algorithm uses the principles of Kalman filter [13].
The algorithm predicts the location of the next track point based on the current state
which is updated after each new point addition.

Let us consider the technique of the algorithm in more detail. The algorithm oper-
ates sequentially with all snapshot pairs. For each snapshot, the pixels with a large
number of counts are selected. As soon as we have a set of selected pixels the algo-
rithm attempts to connect all possible pairs of pixels between two snapshots into
track segments. Thus it tries to connect all pairs of points, which satisfy criteria of
distance, duration and deviation from track line. If a point satisfies all the criteria it
is added to the track. As soon as the track contains more than two pixels, it is fitted
with a line on each step. The line is used in "deviation from track line" criterion.
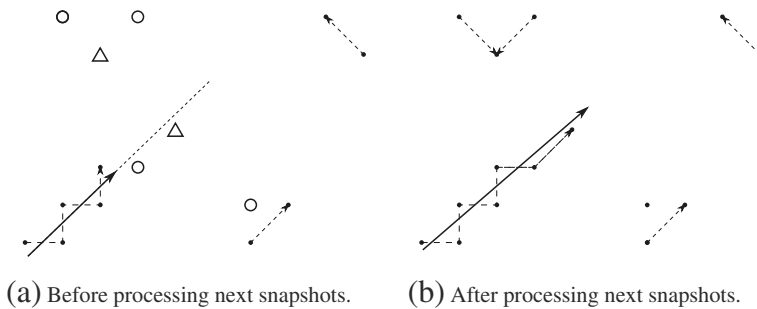
(a) Before processing next snapshots.    (b) After processing next snapshots.

**Fig. 4** The scheme of track finding method. Figure 4a represents three already found tracks (*dashed lines*), with their pixels (*black dots*) and a fitted line for the track containing more than 2 pixels. Selected pixels which will be added to the tracks on next iterations are drawn with circles (+1 GTU) and triangles (+2 GTU). Figure 4b represents the same set of data, but after the addition of new pixels: two more short tracks are found, one track is extended and one pixel is ignored since it's not matched to any track

In Fig. 4, the rough scheme of the algorithm is shown. Track candidates are not only selected from two consecutive snapshots: the algorithm is able to look back for 5 GTU in order to find track segments.

The algorithm does not distinguish between the signal and background pixels. However, the background pixels are distributed randomly and the probability of these pixels to be connected into a single track decreases vastly with the track length. Occasionally, a background pixel can be added to the signal track and spoil it. The problem is solved by saving the track before adding the point. The background pixel is added only in one of the two. The addition the background pixel changes the condition of the next pixel selection. The track with the background pixel develops in a different way than the track without. The background pixel deviates the test track from the true track, thus this track has less probabillity for signal pixels to be added in the next steps. This method provides a way of continuing the track reconstruction even after the addition of a background count.

In the end of the procedure, we have a large set of tracks. Nearly the entire set is composed of shorts tracks, which are caused by the accidental coincidence of background pixels, as well as the fragments of the signal track, that are "spoiled" by the addition of background pixels. The signal track is selected as a track with the highest number of counts: it corresponds to the longest found, straight track with the highest signal and containing no time leaps. In Fig. 6 , the result of the algorithm application to a Monte Carlo event is shown.

Further, one can define the selection criteria that are used in the algorithm in more detail:

**Pixel selection**    The number of selected pixels in each step is an adaptive quantity: the number of selected pixels with same number of counts ( dashed blue line in the Fig. 5 ) on each snapshot should be less then 32. In Fig. 5, the average distribution of p. e. counts (photon-counts) for signal and background pixels for events with energies $7 \times 10^{19}$ and $3 \times 10^{20}$ eV and zenith angles 30° and 75° are shown. One can see that the chosen cut on number of counts selects a big portion of background
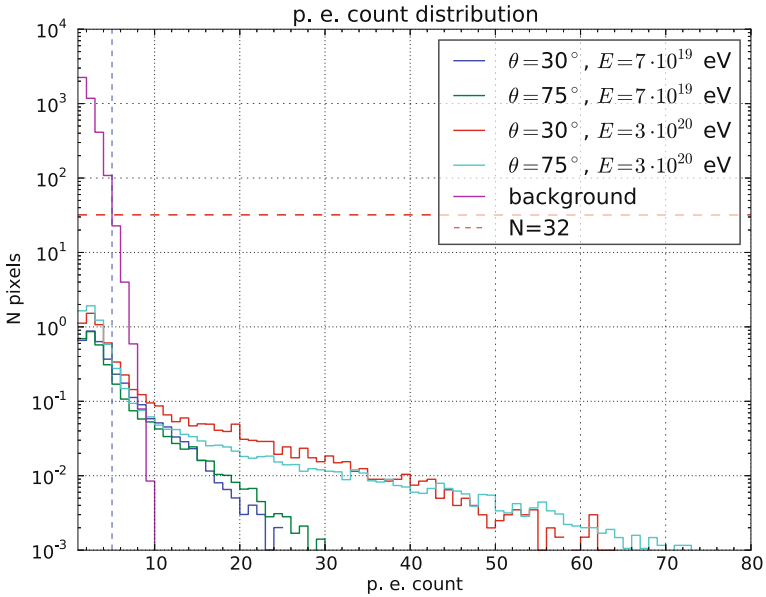
**Fig. 5** The distribution of p. e. counts (photon-counts) for signal and background pixels for events with energies $7 \times 10^{19}$ and $3 \times 10^{20}$ eV and incident angles 30° and 75°. *Dashed red line* represents the chosen cut on number of counts

pixels in addition to the signal ones: the main purpose of this cut is to limit the number of track candidates in memory.

**Distance** In the beginning of the procedure the maximal distance between two connected pixels is equal to 2 pixel diagonals. If the track's average velocity exceeds one pixel diagonal per GTU, the additional cut on distance is applied: the distance to the new pixel divided by delta GTU should be less than doubled track velocity.
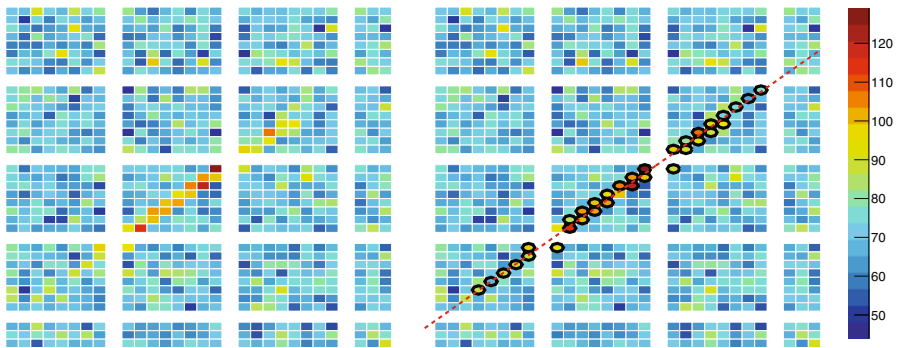


**Fig. 6** The integrated signal on the focal surface from EAS with $E = 1 \times 20$ eV and $\Theta = 60°$. The pixels selected by the algorithm are marked with black circles. The dotted red line represent the obtained track line. The color of each pixel corresponds to the p. e. counts

**Duration**    The duration between two connected pixels should be less than 5 GTU. This number is based on the geometry of the focal plane and velocity of the track: the gap between photomultipliers is not large enough to produce a delay in signal of more than 5 GTU.

**Deviation from the track line**    A distance between the pixel and the fitted line should be less than 2 pixels in size (Fig. 6).

The constants for this algorithm are chosen based on geometrical estimations and in the future can be tuned based on simulation results.

## 2.3 LTT-PreClustering

Speed and precision of modules such as described above can be further enhanced when the *linear tracking trigger pre-clustering* (LTT-PreClustering) is applied prior to the actual pattern recognition. In analogy to the trigger algorithm on-board the instrument, this technique can be used to make a pre-selection of the data. It selects the pixels on the focal surface containing the highest number of counts. Then it searches for the track that maximizes counts by moving an integration box along a pre-defined set of directions intersecting this point. All pixels that are not part of the selected area are hidden from the following pattern recognition module. Thus accumulations of pixels that could potentially be mistaken as part of the signal are excluded from further analysis.

## 3  Angular reconstruction

After signal discrimination, the basic information to reconstruct the geometrical properties of the EAS is handed over to the track direction module. This is the signal track on the focal surface, i.e. number of detected photons and their timing information, as well as their arrival direction $\theta^{FOV}$ and $\phi^{FOV}$ to the instrument. The shower direction is described by a unit vector $\hat{\Omega}(\Theta, \Phi)$ with its origin at the shower core (impact position on ground) pointing along the shower axis into the sky (see Fig. 7).

$$\hat{\Omega} = \begin{pmatrix} \sin\Theta\cos\Phi \\ \sin\Theta\sin\Phi \\ \cos\Theta \end{pmatrix} \qquad (2)$$

### 3.1 Reconstruction of the track detector plane

The first step of the angular reconstruction is the estimation of the Track Detector Plane (TDP), also referred to as Shower Detector Plane (SDP). This is the plane which contains the shower track and the detector itself (see Fig. 7). Its position can be inferred from a x-t and a y-t fit of the signal track. The TDP is determined by its normal $\hat{V}$, given by:

$$\sin(\alpha_{ij})\hat{V} = \hat{n}_i \times \hat{n}_j \qquad (3)$$

here $\hat{n}_i$ and $\hat{n}_j$ denote the unit vectors pointing from the detector to the ith point $P_i$ of the EAS and the $j^{\text{th}}$ point $P_j$ respectively, and $\alpha_{ij}$, the angle between $\hat{n}_i$ and $\hat{n}_j$.
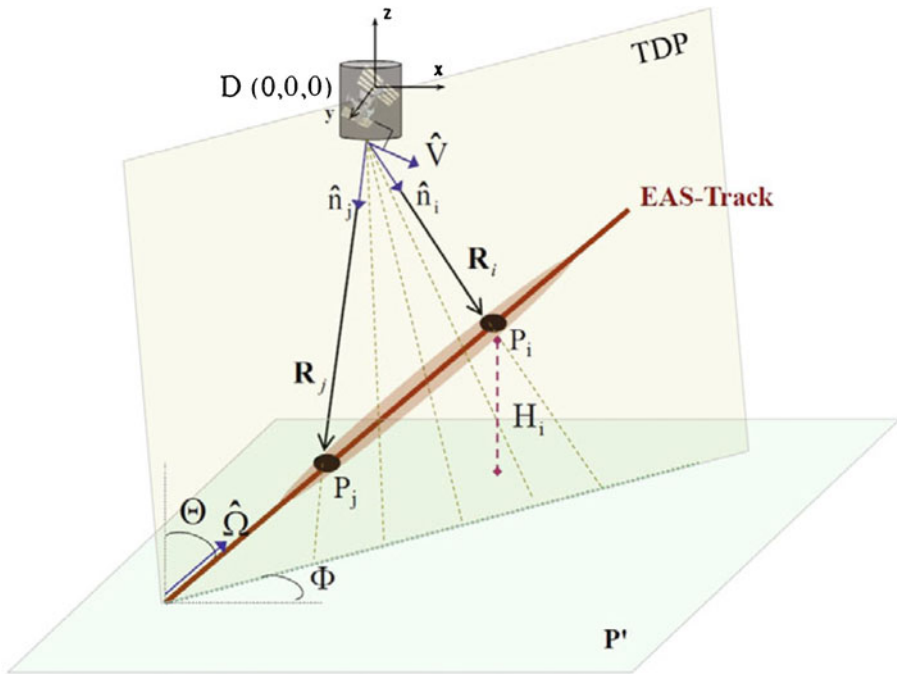
**Fig. 7** Schematic sketch of the geometrical relations used in the track reconstruction: $\hat{\Omega}(\Theta, \Phi)$, the arrival direction of the UHECR is linked to the geometrical position of the signal track on the detector's focal surface by the position of the TDP. One arbitrary point $P_i$ on the EAS is connected to the detector by the vector $R_i$, its height above the ground is denoted by $H_i$. From another point $P_j$ the vector $\mathbf{L}_{ij}$ points back to $P_i$. The line of intersection of the TDP with the ground is called rtdp [6]

An alternative technique to determine the TDP is based on $\hat{n}_i$, the unit vector pointing to the shower maximum $\hat{n}_{\max}$. Then $\hat{V}$ can also be defined as:

$$\hat{V}_i = \frac{\hat{n}_i \times \hat{n}_{\max}}{\sin(\alpha_i)} \tag{4}$$

where $\alpha_i$ is the angle between $\hat{n}_{\max}$ and $\hat{n}_i$. The normal $\hat{V}$ defining the TDP (with azimuthal and polar angles $\theta_{\hat{v}}$ and $\varphi_{\hat{v}}$), is found by maximizing the sum of the scalar products of $\hat{V} \cdot \hat{V}_i$: $C = \sum_i (\hat{V} \cdot \hat{V}_i)$. All $\hat{V}_i$ are chosen to point in the same half-sphere where all scalars have the same sign. This can be done analytically by equating the first derivatives of $C$, with respect to $\varphi_{\hat{v}}$ and $\theta_{\hat{v}}$ to zero. Thus the TDP is given by the following equations:

$$\varphi_{\hat{v}} = \arctan\left(\frac{\sum_i \frac{n^i_y}{\sin \alpha_i}}{\sum_i \frac{n^i_x}{\sin \alpha_i}}\right), \theta_{\hat{v}} = \arctan\left(\frac{\sum_i \frac{n^i_\perp}{\sin \alpha_i}}{\sum_i \frac{n^i_z}{\sin \alpha_i}}\right) \tag{5}$$

where $n^i_x$, $n^i_y$, $n^i_z$, $n^i_\perp$ are components of $\hat{V}_i$ on a right handed coordinate system with its origin at the detector (see Fig.7).

## 3.2 Track reconstruction algorithms

Most of the track reconstruction algorithms rely on the determination of the TDP. Knowing its position, the task of the algorithm of choice is to determine $\beta$, the angle between $\hat{\Omega}$ and $\hat{W}$. $\hat{W}$ is the unit vector perpendicular to $\hat{V}$ and parallel to a plane tangent to the earth's surface (see Fig. 8). From $\beta$ the calculation of $\hat{\Omega}$ and, therefore, $\Theta$ and $\Phi$ is straightforward:

$$\hat{\Omega}(\Theta, \Phi) = \hat{W} \cos(\beta) + \hat{V} \sin(\beta) \tag{6}$$

To compute $\beta$, the unit vector $\hat{n}_{max}$ pointing from the telescope towards the maximum of the shower, the altitude of the maximum $\mathbf{H}_{max}$ and the *core position* $P_c$ are needed.

Considering the two points $P_i$ and $P_j$ on the shower axis, the length of the segment between these two points, $|\mathbf{L}_{ij}|$, can be expressed by (see Fig. 7):

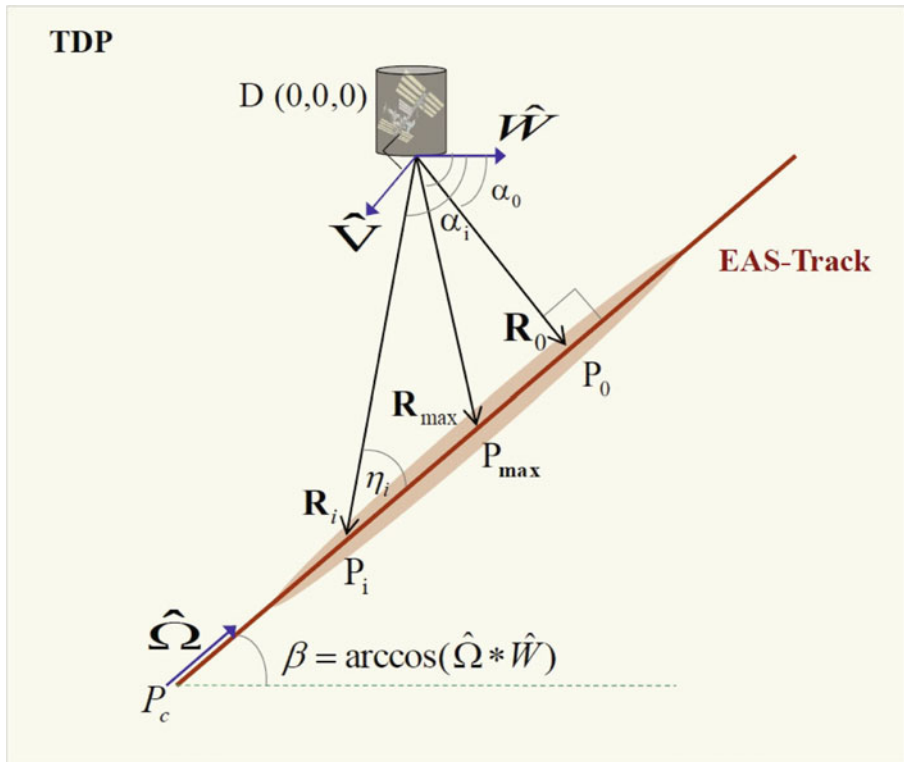$$|\mathbf{L}_{ij}| = |\mathbf{R}_i - \mathbf{R}_j| = c\Delta t_{shower} \tag{7}$$



**Fig. 8** Illustration of the TDP and the important vectors $\hat{n}_i$ and $\hat{V}$ for its reconstruction. The point $P_0$ is the closest point of the shower to the detector, $P_{max}$ indicates the position of the fluorescence light maximum. If the TDP position in terms of $\hat{V}$ and $\hat{W}$ is known, $\beta$ allows to calculate $\hat{\Omega}(\Theta, \Phi)$ [6]

In this last expression, $\Delta t_{shower}$ is the time between the emission of the light at points $P_i$ and $P_j$, respectively. Thus $\Delta t$, defined as the time elapsed between the detection of the photons coming form points $P_i$ and $P_j$, is given by:

$$\Delta t = t_i - t_j = \Delta t_{shower} + \frac{|\mathbf{R}_i| - |\mathbf{R}_j|}{c} \tag{8}$$

$$= \frac{|\mathbf{L}_{ij}|}{c} + \frac{|\mathbf{R}_i| - |\mathbf{R}_j|}{c} \tag{9}$$

The speed of the particles is hereby assumed as the speed of light $c$. Now, going from the general coordinate system of Fig. 7 to the one in the TDP (Fig. 8), this relation is expressed as a function of $\alpha$ and $\beta$

$$t_i = t_j - \frac{R_j}{c} \left[ \frac{\sin(\alpha_j - \alpha_i) + \sin(\alpha_i + \beta) - \sin(\alpha_j + \beta)}{\sin(\alpha_i + \beta)} \right] \tag{10}$$

A set of different techniques is implemented in ESAF to reconstruct the shower direction.

1. the *analytical approximate algorithm AA1* uses the angular velocities of the signal track in the x-z and y-z planes. The velocity is approximated by a linear fit, assuming the speed as a constant, as explained in Section 3.1
2. the *analytical approximate algorithm AA2* here the shower speed is approximated as a constant on a plane $p$, tangent to the earth's surface.
3. the *numerical exact algorithm NE1* performs a $\chi^2$ minimization of the difference between the arrival times of photons $t_i$ to the detector and the ones coming from a test shower track theoretically computed at the minimal distance $\mathbf{R}_p$, between the shower and the detector.
4. the *numerical exact algorithm NE2* performs a $\chi^2$ minimization of the difference between unit vectors $\hat{n}_i$ derived from the selected pixel on the detector, and the unit vectors derived from a test track. It works without prior knowledge of the TDP. Still the selected pixel are provided by the pattern recognition.
5. the *numerical exact algorithm NE3* determines $\hat{\Omega}$ and $H_{\max}$ by minimizing the function $F$ representing the difference between a set of measured unit vectors of the photons arrival direction $\hat{n}_i$ and its expectation $\hat{n}'_i$. The algorithm uses the identification of the shower maximum and the TDP.

A detailed description of the derivation of the algorithms can be found in [20, 22] and references therein.

### 3.2.1 Analytical approximate algorithm AA1

This method is executed at the beginning of every reconstruction run. Its results can either be used exclusively or as a starting point for one or some of the following methods. Inside the TDP, it works in an iterative way with the help of the identification of the fluorescence light maximum. Both approximate methods, explained in the following, use the reconstruction of the TDP and the identification of the shower

maximum. $\beta$ can be obtained by differentiating (10) with respect to $\alpha_i$ and approximating the angular velocity of the signal on the focal surface as constant. This is valid due to the relatively large distance of the signal from the detector. Thus

$$\beta = 2 \arctan \left( \frac{c}{\omega \cdot R_{max}} \right) - \alpha_{max} \tag{11}$$

The angular velocity $\omega$ is the slope of the line which is obtained from the fit of $\alpha(t)$. The distance $R_{max}$ between the detector and the shower maximum can be calculated by using the height of the shower maximum $H_{max}$:

$$R_{max} = (R_\oplus + H_{ISS}) \cdot \cos \Theta_{max}$$
$$- \sqrt{(R_\oplus + H_{max})^2 - ((R_\oplus + H_{ISS}) \cdot \sin \Theta_{max})^2} \tag{12}$$

where $R_\oplus$ denotes the earth radius. $H_{max}$ has to be guessed with an initial value of 5 km in the first place. This can be done because the error of this initial $H_{max}$ is small compared to $H_{ISS}$. Moreover, in the next iteration step it is replaced with a more precise value. The shower maximum is derived from a Gaussian fit of the $N^{Hits}(t_i)$ distribution, where $N^{hits}(t_i)$ is the number of photons on the selected pixel at time $t_i$. Now, a first value for $\beta$ can be calculated by using (11). After that, $H_{max}$ is recalculated by

$$H_{max} = c \cdot \log \left[ \frac{(X_{max} \cdot \cos \Theta - a)}{b} \right] \tag{13}$$

$X_{max}$ is approximated as 831 g/cm$^2$ in the first place, the parameters a,b,c come from a lookup table based on experimental data of the US Standard Atmosphere. With the new $H_{max}$ and $\beta$, $\Omega$ can eventually be recalculated, which finally yields the reconstructed shower direction.

### 3.2.2 Analytical approximate algorithm AA2

AA2 also relies on the knowledge of the TDP. This time the speed of the shower is approximated as constant on a plane $p$ tangent to the earth's surface and perpendicular to the detector.

$$V_{xy} = \sqrt{V_x^2 + V_y^2} \tag{14}$$

Using (9) and (10) and assuming $\alpha_i \approx \alpha_{max}$, we arrive at the following expression for $\eta_{max}$ (see Fig. 8 ):

$$\eta_{max} \simeq 2 \arctan \left( \frac{V_{xy}}{c} \sin \alpha_{max} \right) \tag{15}$$

using $V_{xy}$ as derived above, $\beta$ yields

$$\beta = \pi - \eta_{max} - \alpha_{max} \tag{16}$$

As in AA1, the shower incoming direction can be computed by (6).

### 3.2.3 Numerical exact algorithm NE1

For each pixel on the focal surface that is active, a set of basic information is available: $\hat{n}_i$, $t_i$, $N^{hits}(t_i)$, describing the arrival direction of the photons from the shower, their arrival time and the number of photoelectrons produced in the pixel. The exact technique described here, aims at finding the geometrical properties of the air shower by comparing the photon's arrival angles measured, to those theoretically computed. This technique works without the need to reconstruct the TDP in advance. A first starting value for $\beta$ is inherited from either AA1 or AA2. Then, for each shower point $P_i$, the procedure calculates the arrival times of the photons to the instrument.

$$t_i^{exp} = t_{max} - \frac{R_{max}}{c}\left[\frac{\sin(\alpha_{max} - \alpha_i) + \sin(\alpha_i + \beta) - \sin(\alpha_{max} + \beta)}{\sin(\alpha_i + \beta)}\right] \quad (17)$$

By minimizing the $\chi^2$ function

$$\chi^2(t_i) = \sum_{i=1}^{n\,pixel,gtu} \frac{(t_i^{measured} - t_i^{exp})^2}{\sigma_i^2} \cdot N^{hits}(t_i) \quad (18)$$

a more precise value for $\beta$ can be computed.

### 3.2.4 Numerical exact algorithm NE2

This method is comparable to the NE1. However, in this case, matching the 'test track' to the measured signal is done by comparing the arrival angles of the photons to the detector. Starting from one known point of the signal track, either the Cherenkov mark $P_c = (x_c, y_c, z_c)$, or if it is not possible to spot or to identify it (the more general case), the last point of the shower measured, assuming it hits the ground at this position. For initial test values of $\Theta$ and $\Phi$, a generic point $P_i(\Theta, \Phi, t_i)$ on the test track (also intersecting $P_c$) can be computed (see Fig. 9) that corresponds to the arrival time at the telescope $(t_i - t_c)$. We can express $\beta'$ by the distance $(R_c)$ to $P_c$ and $t_i$

$$\beta' = 2arccot\left(\frac{c(t_i - t_c)}{R_c \sin\theta'} + \cot\left(\frac{\theta'}{2}\right)\right) \quad (19)$$

and for $\theta'$ we can write

$$\theta' = \arccos\left(\frac{\mathbf{R_c}}{|\mathbf{R}_c|} \cdot \hat{\Omega}(\Theta, \Phi)\right) \quad (20)$$

For every pixel $\psi_i$, the angle between $\hat{n}_i^{measured}$ and $\hat{n}_i^{test} = \frac{\mathbf{R}_i^{test}}{|\mathbf{R}_i^{test}|}$, can be computed.

$$\psi_i(\Theta, \Phi) = \arccos\left(\hat{n}_i^{measured} \cdot \frac{\mathbf{R}_i^{test}}{|\mathbf{R}_i^{test}|}\right) \quad (21)$$

Therefore, the $\chi^2$ function to be minimized is

$$\chi^2(\psi_i) = \sum_{i=1}^{n\,pixel} \frac{\psi_i^2(\Theta, \Phi)}{\sigma_i^2} \cdot N_i^{hits}(t_i) \quad (22)$$
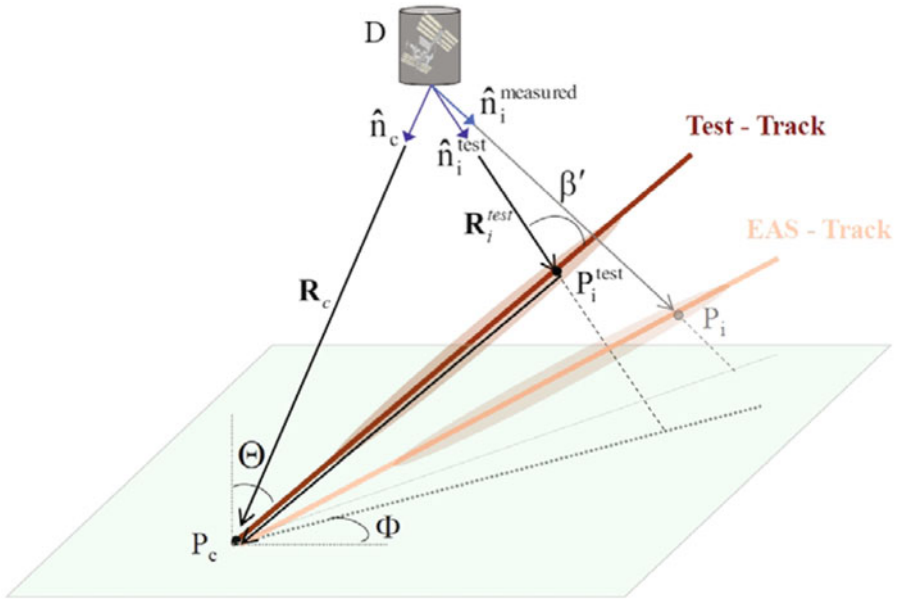
**Fig. 9** Orthogonal reference system, origin at sea level on the nadir of the detector. $P_i$ is some generic point of the track, $P_c$ the known point of the track, p' is a plane perpendicular to z. The test track also intersects $P_c$. By variation of its arrival angles $\Theta$ and $\Phi$, the $\chi^2(\psi_i)$ function can be minimized [6]

The weight $N_i^{hits}$ is the number of photons on the i$^{th}$ pixel. $\sigma_i$ is constant and equal to the field of view of a pixel ($\approx 0.1°$). Derivations of the formulas can be found in [22] and references therein.

### 3.2.5 Numerical exact algorithm NE3

Once the TDP is found, the task of finding the 3-dimensional shower direction vector $\hat{\Omega}$ is reduced to the 2-dimensional case with a single parameter $\beta'$. As one can see from Fig. 9, the $\beta'$ is the plane angle between the vector that points to shower maximum $\hat{R}_{max}$ and shower direction $\hat{\Omega}$. The shower direction vector $\hat{\Omega}$ can be found by rotating the unit vector to the first point of the shower $\hat{n}_{max}$, around the calculated $\hat{V}(\theta_{\hat{V}}, \varphi_{\hat{V}})$ (5) by an angle $\beta' - \pi$. The expected value of $\hat{n}_i' = \frac{\mathbf{R}_i'}{|\mathbf{R}_i'|}$ can be obtained by:

$$\mathbf{R}_i' = \mathbf{R}_{max} + L_i \hat{\Omega}, \tag{23}$$

where $L_i$ is the distance between the shower maximum and point $P_i$. Thus $L_i$ is related to $t_i - t_{max}$ by:

$$L_i = c\Delta t + |\mathbf{R}_{max}| - |\mathbf{R}_i'| \tag{24}$$

with $t_i$ and $t_{max}$ being the times of arrival of the photons at the focal plane. The length of the expected vector $\mathbf{R}'_i$ can be found by taking the square of (23) and substituing from (24). Thus $|\mathbf{R}'_i|$ is given by the following equation:

$$|\mathbf{R}'_i| = \frac{\left( \mathbf{R}_{max} + \hat{\Omega} \left( c\Delta t + |\mathbf{R}_{max}| \right) \right)^2}{2 \left( \mathbf{R}_{max} \cdot \hat{\Omega} + c\Delta t + |\mathbf{R}_{max}| \right)} \tag{25}$$

The distance $R_{max}$ between the detector and shower maximum can be obtained using (12). The altitude of the EAS maximum is $H_{max}$ is computed using the relation between the time width of the signal on the focal plane $\sigma$ and the air density $\rho \left( H_{max}^{fluo} \right)$ in the atmosphere at which the EAS develops [3]:

$$\sigma = \sqrt{2\xi_{max}} \frac{X_0 \left( 1 + \hat{n}_{max} \cdot \hat{\Omega} \right)}{\rho(H_{max}^{fluo})c} \tag{26}$$

$$\xi_{max} = a + b \ln \left( E/E_c - \ln A \right) \tag{27}$$

This equation was obtained using the GIL parametrization for the longitudinal development of the number of charged particles. $\xi_{max}$ is a dimensionless parameter, $E$ is
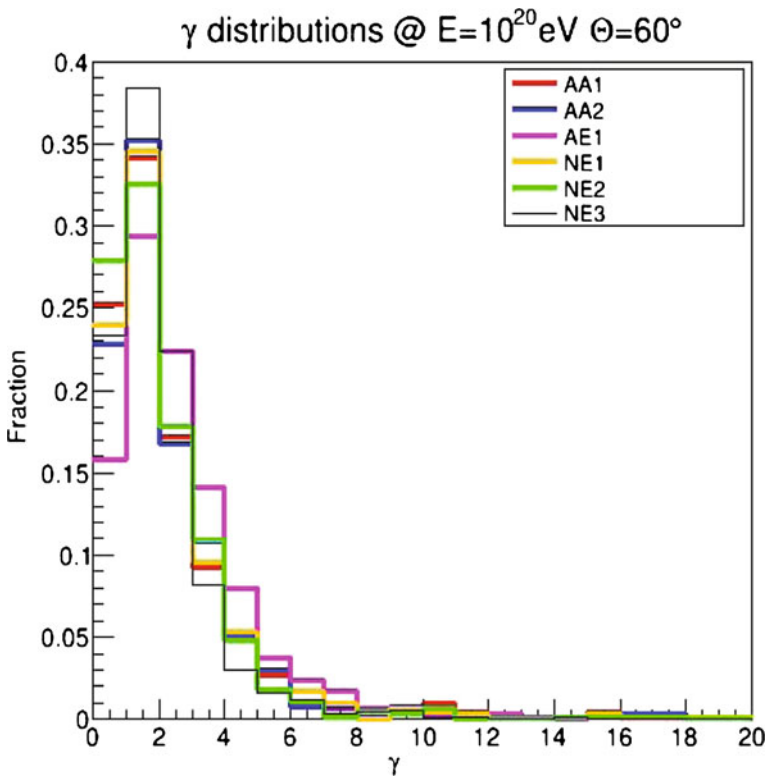


**Fig. 10** Distribution of the angular difference between input and reconstruction angles ($\gamma$) for different algorithms. In all cases the simulated primary was a proton with an energy of $10^{20}$eV and $\Theta = 60°$

the energy of the primary particle, $A$ — its atomic number, $X_0 = 37.15 \ g/cm^2$ — the air radiation length, $E_c = 81$ MeV (critical energy), $a = 1.7$ and $b = 0.76$. These values are chosen based on CORSIKA-QGSJET-II results [14].

Considering that parameter $\xi_{max}$ depends on UHECR energy logarithmically, it can be taken into account in an iterative procedure, or the energy can be set to a mean expected value. The $\sigma$ can be estimated from the information about the signal or can be assumed as a minimization parameter. As soon as we calculate $\rho\left(H_{max}^{fluo}\right)$, the altitude of the EAS maximum becomes known. This method is used as an algorithm to reconstruct the shower maximum. It is correct for any kind of particle.

Thus we have two minimization parameters $\beta'$, which along with the TDP, determines $\hat{\Omega}$ and $\rho\left(H_{max}^{fluo}\right)$ which determines $H_{max}$. Since the expected value of the
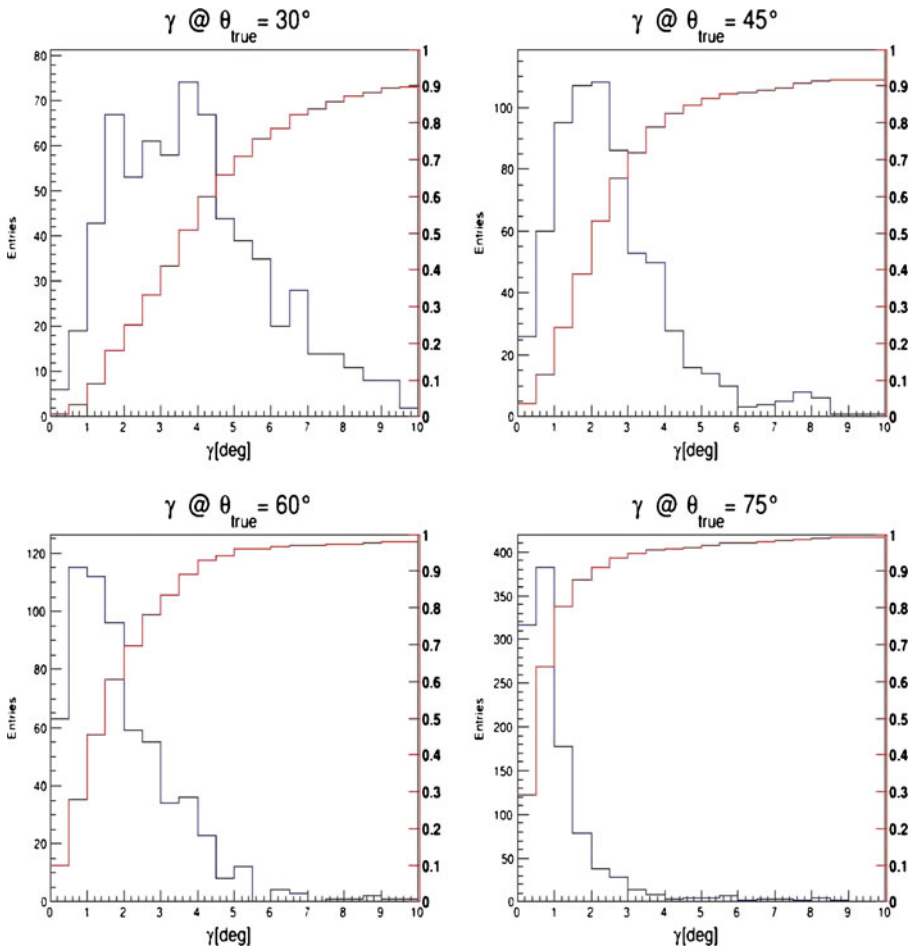


**Fig. 11** Distribution of the angle($\gamma$) between input and reconstructed directions for different zenith angles. In *red*, the cumulative distribution is shown. All simulated showers had a proton primary with E=$10^{20}$ eV. For the two upper plots the NE3 algorithm was used, while the NE2 algorithm was used in the lower two

photons arrival direction $\hat{n}_i' \left( \theta_{\text{expected}}^{\text{FOV}}, \phi_{\text{expected}}^{\text{FOV}} \right)$ is computed, we can minimize the $\chi$ function, that is defined as:

$$\chi = \sum_{i=1}^{n_{gtu}} \frac{(\hat{n}_i - \hat{n}_i')^2 \, N_i^{\text{p.e.}}}{\left( \sigma_{\Delta t}^2 + \sigma_{\text{pix}}^2 \right)_i}, \qquad (28)$$

where $\sigma_{\Delta t} = |\hat{n}_{i+1} - \hat{n}_i| = \sqrt{2(1-\cos\alpha)}$ is calculated as variation of $\hat{n}_i$ within time of 1 GTU, where $\alpha$ is angle between $\hat{n}_{i+1}$ and $\hat{n}_i$. Pixel efficiency is not uniform across the photon incident angle. The error calculation should be based on the width of pixel efficiency vs. incident angle distribution, which is indeed smaller than total pixel FOV. $\sigma_{\text{pix}} = \sqrt{2(1-\cos\kappa)}$ is calculated as the variation of $\hat{n}_i$ inside a single pixel field of view $\Omega_{FOV}^{pix}$, and $\kappa$ is the solid angle that one can calculate using following equation $\kappa \approx \sqrt{4\Omega/\pi}$. Currently we use maximal deviation of the arrival direction vector within 1GTU. Thus both assumptions overestimate the real error and will be improved in future.

## 4 Reconstruction of UHECR's arrival direction: statistical studies

### 4.1 Data sample

The library of UHECR events used in this study to evaluate the angular reconstruction performance has been simulated under the following conditions: Our primary
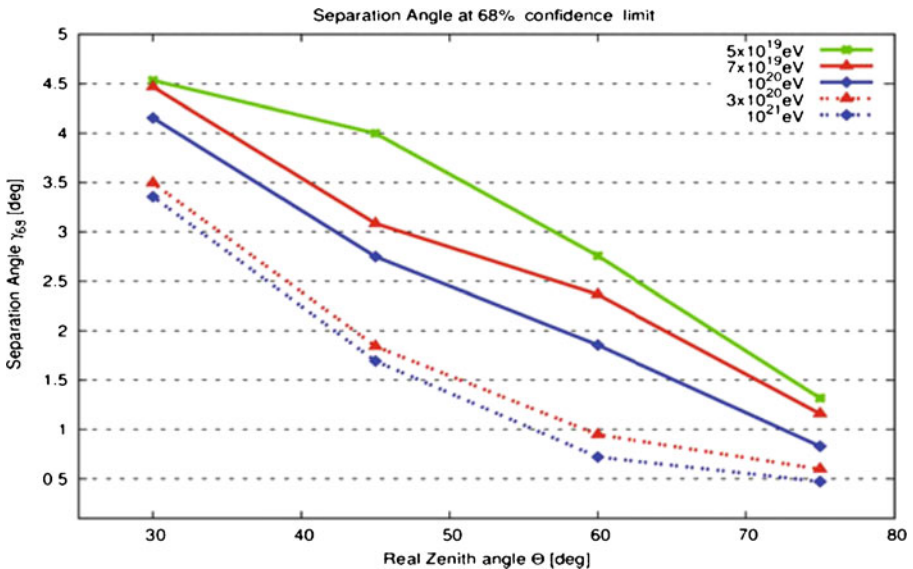


**Fig. 12** $\gamma_{68}$ for all the energy and $\Theta$ configurations in our simulated data sample (see text)

particles are protons. We simulate a combination of five different energies ($E = 5 \times 10^{19}eV, 7 \times 10^{19}eV, 10^{20}eV, 3 \times 10^{20}eV$ and $10^{21}eV$,) and four zenith angles ($\Theta = 30°, 45°, 60°$ and $75°$). The altitude of the ISS has been assumed to be 400 km. The distribution of charged particles during the shower development is parametrized with the GIL function [12]. Fluorescence yield has been parametrized according to [18]. We have used the US Standard 1976 atmosphere [23]. For propagation of light in the atmosphere, we are using a parametrized approach, taking into account second order scattering of the Cerenkov light. The background rate originated from night glow has been assumed to be 500 photons $ns^{-1}m^{-2}sr^{-1}$, the earth's albedo 5 % [7].

In the studies presented here, the position of the maximum and the number of pixels selected by the pattern recognition have the biggest impact in our reconstruction. The selection criteria will be discussed in Section 4.3. As discussed in [1], there are many factors that reduce the trigger rate. For all the results herein presented, we only reconstruct EAS if they activated the trigger algorithms during their simulation in ESAF. Therefore, the reconstruction techniques developed and tested here, were done assuming good observation conditions.
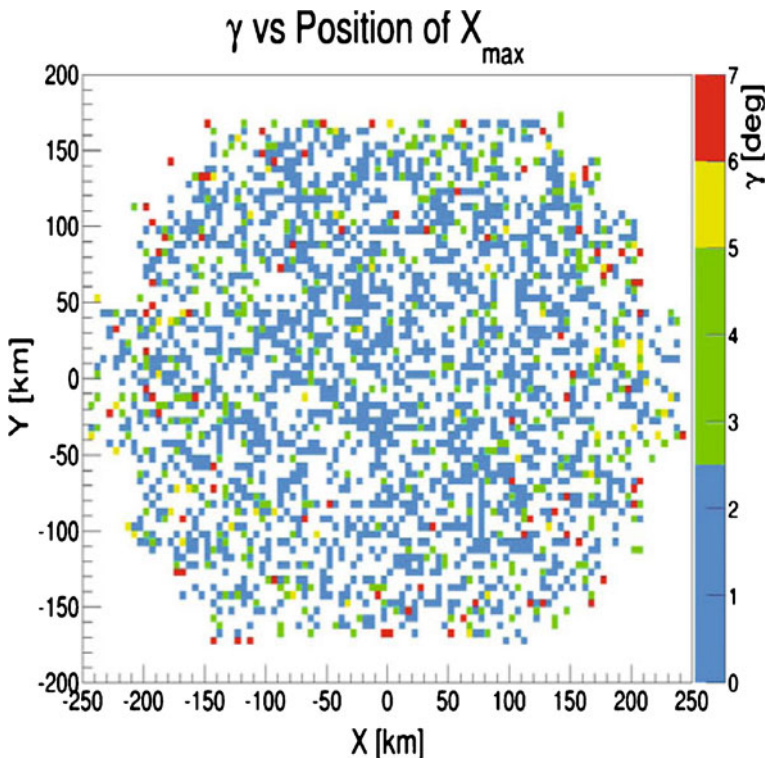


**Fig. 13** The positions of the shower maximum projected on the ground. The color scale repres the value of $\gamma$: *blue* for $\gamma < 2.5°$, green for $2.5° \leq \gamma < 5°$, *yellow* for $5° \leq \gamma < 6°$, and *red* for $6° \leq \gamma$. In this plot we show results for proton showers with an energy of $10^{20}$eV, including all zenith angles from our data sample

## 4.2 Angular resolution

To estimate the expected angular resolution of JEM-EUSO, we compared the angle ($\gamma$) between the injected shower axis and the reconstructed one. We define $\gamma_{68}$ as the value at which the cumulative distribution of $\gamma$ reaches 0.68. It is worth mentioning that both systematic errors and statistical fluctuations are included within the definition of $\gamma_{68}$. We will use this parameter as a measurement of the overall performance of our reconstruction capabilities. In Fig. 10 we show the $\gamma$ distribution of all algorithms. In this particular example we only reconstructed proton initiated EAS with an energy of $10^{20}$eV and $\Theta = 60°$. As it can be seen, for all algorithms the maximum of the distribution lies between 1° and 2°.

In Fig. 11, we show $\gamma$ distributions for simulated proton showers with a primary's energy of $10^{20}$eV. Since JEM-EUSO is observing the EAS's track from above, the more vertical the EAS, the harder it will be to reconstruct it (e.g. $\theta \leq 45°$). This complication arises since these EAS are seen by relatively less pixels than an EAS more parallel to the ground(more inclined showers). The expected angular resolution without any selection cuts is shown in Fig. 12.
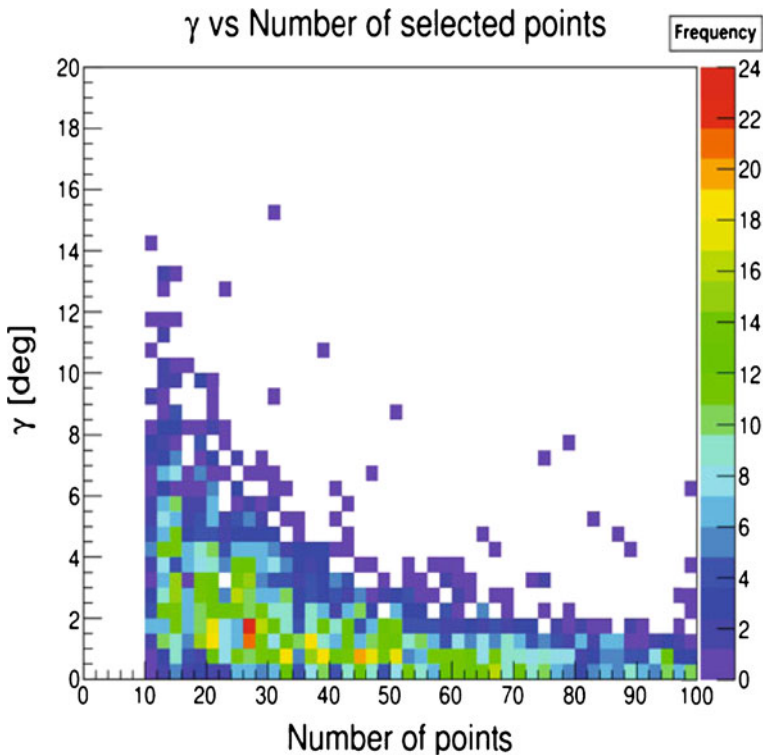


**Fig. 14** $\gamma$ dependence on the number of points selected by the pattern recognition module. The frequency is color coded. In this plot we show results for proton showers with an energy of $10^{20}$eV, including all zenith angles from our data sample

### 4.3 Selection criteria

To talk about an overall reconstruct-ability of the UHECR is a bit misleading, as it depends on many intervening factors. This concept must be defined within clearly delineated observation conditions. Therefore, we introduce the following selection cuts:

- $X_{max}$ **position**. This is the position relative to JEM-EUSO's field of view where the simulated EAS's maximum occurred. In Fig. 13, we can see that there is an excess of poorly reconstructed showers at the edge of the FOV.
- **Number of points (Track length)**. The number of points selected by the pattern recognition module. The term *"points"* is used in the general sense of a fitting procedure. In other words, if the same pixel is selected by the pattern recognition in several GTUs, it will provide several *"points"* to the fitting algorithms. This criterion is a measurement of the information available for the angular reconstruction techniques. The impact of this criterion is shown in a 2D histogram in Fig. 14.

Before we discuss in more detail the impact of these cuts in the quality of the angular reconstruction, let us remember that they are not independent. It is often the case that these selection cuts are correlated. For example, the triggering probability has a correlation with the injection position which is directly related to the position of the maximum.

EAS developing near the border of the FOV of JEM-EUSO may not be completely contained within the FOV depending on the specifics of each EAS. This will translate
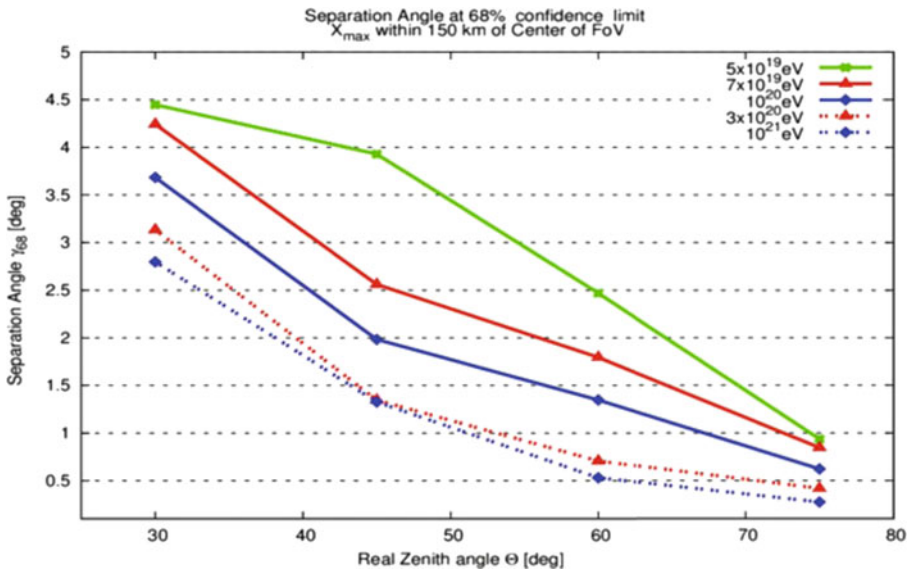


**Fig. 15** $\gamma_{68}$ imposing the condition that the maximum of the shower was less than 150 km from the center of the field of view

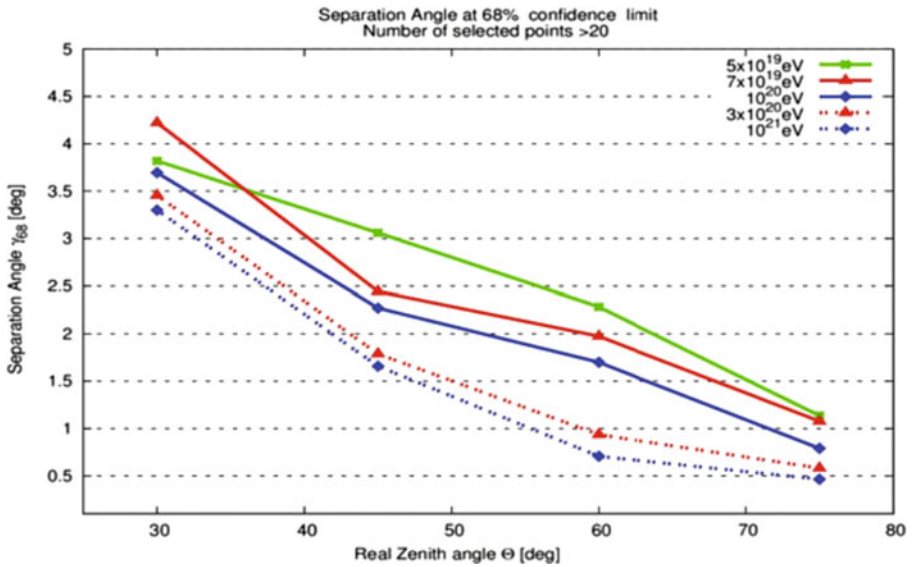**Fig. 16** $\gamma_{68}$ imposing that at least 20 points were selected by the pattern recognition algorithm

into an incomplete shower track and a loss of information. On a second hand, the area observed by the pixels on the outer parts of the FOV is bigger and this diminishes the angular reconstruction's accuracy [1]. The resolution for events, whose $X_{max}$ is within 150 km from the center of the FOV, is shown in Fig. 15.

Finally, for the number of points selected by the pattern recognition (track length), we show the angular resolution selecting events with at least 20 points selected by the pattern recognition on Fig. 16.

## 5 Discussion and outlook

Using the advanced ESAF software with the JEM-EUSO detector, we have conducted a high statistics study on the angular reconstruction capabilities of the JEM-EUSO mission. Protons with energies, reaching from $5 \cdot 10^{19}$ eV up to $10^{21}$ eV together with different zenith angles have been simulated, reconstructed and analyzed. We have evaluated the quality of the reconstructed events with respect to different point of views. We have addressed the question of the expected overall performance of the detector. For the case of primaries with energies of $10^{20} eV$ and $\Theta = 60°$, we reconstructed at least 95 % of the triggered events. This number is a lower limit on the capabilities of the reconstruction, since at this stage the algorithms and selection mechanisms are still being optimized. On the other hand, by selecting subsamples of events by imposing selection cuts or limiting the focal surface area, we check for a population of high quality events. Being a fraction of the entire statistics, these events allow for an even more precise analysis of the arrival direction of UHECR.

We can conclude that the present status of the instrument and software already satisfies the scientific requirement [21] of the mission: angular resolution < 2.5° for cosmic rays with energies > $10^{20}$ eV and zenith angles > 60° . Depending on energy and zenith angles, the quality of the reconstructed events allows strong constraints to be placed on existing acceleration models of UHECR. It is important to note that the current results on the telescopes angular resolution do only assess the expected performance of the instrument at the current stage. The real data will be analyzed more carefully. For example, for a given event we will run the algorithms using first the thresholds and then change to progressively more stringent ones; also a comparison between real evens and simulated events, could be used in the future to further refine the resolution. Thus, the actual resolution of the instrument is likely to improve with respect to this estimate. Moreover, cross checking and calibration of the reconstruction techniques, using Xenon flashes and laser beams, is foreseen during operation with the aid of the JEM-EUSO Global Light System [24].

At the moment, we are working towards more refined selection (filtering) mechanisms and improved versions of the angular reconstruction algorithms. We are confident that in the future, the existing algorithms will be enhanced or refined, yielding improved results.

# References

1. Adams, J.H. Jr., et al.: (JEM-EUSO Collaboration): an evaluation of the exposure in nadir observation of the JEM-EUSO mission. Astropart. Phys. **44**, 76–90 (2013)
2. Takahashi, Y., et al.: The JEM-EUSO mission. New. J. of Phys. **11**, 065009 (2009)
3. Berat, C., Bottai, S., De Marco, D., Moreggia, S., Naumov, D., Pallavicini, M., Pesce, R., Petrolini, A., et al.: ESAF: full simulation of space-based extensive air showers detectors. Astropart. Phys. **33**, 221 (2010). arXiv:0907.5275 [astro-ph.IM]
4. Blaicher, M.: End-to-end simulation of the Extreme Universe Space Observatory (EUSO). Bachelor Thesis, Karlsruhe Institute of Technology (2012)
5. Bertaina, M., et al.: For the JEM-EUSO Collaboration: the trigger system of the JEM-EUSO Project. 30th International Cosmic Ray Conference Proceedings (Mérida) (2007)
6. Bertaina, M., et al.: Performances and air-shower reconstruction techniques for the JEM-EUSO mission. Adv. Space Res. (submitted ) (2013)
7. Bobik, P., Garipov, G., Khrenov, B., Klimov, P., Morozenko, V., Shinozaki, K., Bertaina, M., Santangelo, A., Kudela, K., Pastircak, B., Urbar, J.: For the Jem-Euso Collaboration: estimation of JEM-EUSO experiment duty cycle based on Universitetsky Tatiana measurements, 32nd International Cosmic Ray Conference Proceedings (Beijing) (2011)
8. Casolino, M., Kajino, F.: An overview of the JEM-EUSO instrument. This volume of Experimental Astronomy
9. Catalano, O., D'Ali Staiti, G., Gabriele, M., La Fata, L.: 27th International Cosmic Ray Conference Proceedings (Hamburg) 2, 498 (2001)
10. Dagoret, S., Barrillon, P., Jung, A., Ebersoldt, A.: The Photodetector Module of the JEM-EUSO mission. This volume of Experimental Astronomy

11. Ebisuzaki, T., et al.: The JEM-EUSO Project: observing extremely high energy cosmic rays and neutrinos from the international space station. Nucl. Phys. B (Proc. Suppl.) **175–176**, 237–240 (2008)
12. Ilina, N.P., Kalmykov, N.N., Prosin, V.V.: Cerenkov radiation and parameters of extensive air showers. Sov. J. Nucl. Phys. **55**, 1540–1547 (1992)
13. Kalman, R.E.: Trans. ASME–J. Basic Eng. **82D**, 35–45 (1960)
14. Kalmykov, N.N., Ostapchenko, S.S., Pavlov, A.I.: Quark-gluon string model and EAS simulation problems at ultra-high energies. Nucl. Phys. Proc. Suppl. **52B**, 17 (1997)
15. Keilhauer, B., Bohacova, M., Fraga, M., et al.: Eur. Phys. J. Web Conf. **53**, 1010 (2013)
16. Medina-Tanco, G.: Studying individual UHECR sources with high statistics 31st International Cosmic Ray Conference Proceedings (Łódź) (2009)
17. Medina-Tanco, G., Weiler, T., Teshima, M., Ebisuzaki, T., Picozza, P., Santangelo, A., Parizot, E., Bertaina, M.: Science Objectives of the JEM-EUSO mission. 32nd International Cosmic Ray Conference Proceedings (Beijing) (2011)
18. Nagano, M., Kobayakawa, K., Sakaki, N., Ando, K.: New measurement on photon yields from air and the application to the energy estimation of primary cosmic rays. Astropart. Phys. **22**, 235 (2004)
19. Pallavicini, M., the EUSO Collaboration: the extreme universe space observatory. Nucl. Instrum. Methods A **502**, 155–157 (2003)
20. Pesce, R.: Studio ed ottimizzazione delle prestazioni di un apparato per la rilevazione di raggi cosmici di altissima energia dallo spazio. Tesi di Laurea, Universita degli studi di Genova (2004)
21. Santangelo, A., et al.: For the JEM-EUSO Collaboration: requirement and expected performances of the JEM-EUSO mission. 32nd International Cosmic Ray Conference Proceedings (Beijing) 3, 219 (2011)
22. Taddei, E.: Studio di algoritmi per la ricostruzione della direzione deglie sciami atmosferici in EUSO. Tesi di Laurea, Universita degli studi di Firenze (2004)
23. NASA, NOAA, USAF, US-Standard Atmosphere, NASA-TM-X-74335 (1976) NASA, US-Standard Atmosphere Supplements, U.S. Government Printing Office,Washington, D.C., 1976
24. Wiencke, L., et al.: For the JEM-EUSO Collaboration: the JEM-EUSO Global Light System. 33rd International Cosmic Ray Conference Proceedings (Rio de Janeiro) (2013)